

PNAS



Supporting Information for

Melting of non reciprocal solids: how dislocations propel and fission in flowing crystals

Stéphane Guillet, Alexis Poncet, Marine Le Blay, William. T. M Irvine, Vincenzo Vitelli and Denis Bartolo

Corresponding Authors : Denis Bartolo & Alexis Poncet

E-mail : denis.bartolo@ens-lyon.fr, alexis.poncet@ens-lyon.fr

This PDF file includes:

- Supporting text
- Figs. S1 to S5
- Legends for Movies S1 to S6
- SI References

Other supporting materials for this manuscript include the following:

- Movies S1 to S6

Supporting Information Text

1. Experimental methods

We first outline the methods we use to make our microfluidic devices. Next, we describe the methods used to make magnetic Wigner crystals out of microfluidic droplets, and we provide a detailed explanation of the data acquisition and analysis processes.

A. Micro-fabrication.

A.1. Microfluidic stickers. The fabrication of the microfluidic chip follows the protocol described in (1). In short, we use conventional UV lithography techniques to make a master mold of our microchannels (SU8 photoresists). We make a PDMS replica of this geometry (Polydimethyl Siloxane, Silguard) and use the resulting soft stamp to imprint another photosensitive resin NOA81 (Norland Optical Adhesive) to make a micropatterned sticker. We then close the channels by sticking our NOA81 channels on a glass slide of thickness 1 mm. Before starting a series of experiments, the cell is exposed to intense UV radiation in an ozone atmosphere. This step eliminates organic compounds and makes the channel walls highly hydrophilic (2). The stickers are connected to three injection tubes (ETFE Tefzel tubes of inner diameter 1/16") using homemade connectors sealed with epoxy resin at the inlet and outlet of the channel.

A.2. Fabrication of the PDMS Stamp. Creating a microfluidic sticker involves illuminating a photosensitive resin through a PDMS stamp. The first step in making the stamp involves creating a master mold through photolithography, following the protocol in (3). This model is made by depositing negative SU-8 2050 resin (Microchem) on a silicon wafer. Before this, the wafer is heated to 100°C to remove any residual moisture. Then, the substrate and the resin are spin-coated for 10 seconds at 500 rpm and then for 30 seconds at 4000 rpm. They are then baked at 65°C for 3 minutes and then at 95°C for 9 minutes (soft bake). The mask defining the channel geometry is placed between the wafer and a UV-transparent quartz plate, which is then exposed to UV radiations (365 nm, 30 mW/cm²) for 25 seconds. Then, the resin is cured for 2 minutes at 65°C and then for 7 minutes at 95°C. The wafer is cleaned to remove any uncured resin by immersing it in a developer bath for 10 minutes. We finalize the fabrication of the master mold by rinsing it with isopropanol and heating it for 3 minutes at 150°C (hard bake), which eliminates micro-cracks smaller than 5 μ m in size. Finally, we pour 30 grams of PDMS Sylgard 184 from Dow Corning (curing agent 10% mass) the wafer and degas it under vacuum. The mixture is allowed to cure for 2 hours at 72°C. We peel off the PDMS stamp which we use to imprint our $e = 60 \mu$ m deep channels in NOA81 resin.

B. Making a soft Wigner crystal.

B.1. Droplet production. The microfluidic cell includes a T-junction at the inlet for drop generation and advection. We inject the continuous and the dispersed phases in the two inlet channels to form a monodisperse emulsion one droplet at a time at the T-junction. The emulsion is made of Hexadecane droplets dispersed in a continuous phase of ferrofluid (Ferrotec MSG W11 + 0.3%w.t. SDS). The saturation magnetization of MSG W11 is $M_s = 18.5$ mT. We filter the ferrofluid beforehand using 0.22 μ m syringe filters without altering its magnetic properties. The droplets are then advected through a tree network of channels to homogeneously fill the main Hele-Shaw cell in which we conduct our observations. To make droplets of controlled diameter, Figure S1A), we impose the flow rates of the two fluids with a Nemesys Cetoni precision syringe pumps, see Fig. We set the area fraction of the droplets to $\phi^1 = 0.61$ and $\phi^2 = 0.37$ by imposing the flow rates ($Q_{\text{ferro}}^1 = 6 \mu\text{L/min}$, $Q_{\text{Hexadecane}}^1 = 1.5 \mu\text{L/min}$) and ($Q_{\text{ferro}}^2 = 25 \mu\text{L/min}$, $Q_{\text{Hexadecane}}^2 = 2 \mu\text{L/min}$) respectively.

B.2. Crystalization. To organize the droplets into a polycrystal, we use the protocol introduced in (4). We place the microfluidic device in a homogeneous transverse magnetic field \mathbf{B} . We control the strength of the \mathbf{B} field using an electric generator. The magnetic field inside the coil varies linearly with the applied current I , see Figure S1B). We stress that the mean advection velocity of the crystal is independent of the applied magnetic field (Figure S1C).

C. Data Acquisition & Analysis.

C.1. Acquisition. We image our droplet crystals using a Nikon SMZ800 stereo microscope with a 0.5 \times achromatic objective. The chips were positioned at the center of a coil and illuminated with a LED light plate. The experiments were recorded using a 12 Megapixel CMOS camera (Ximea XiC MC124MG-SY). Depending on the injection rates, the duration of the recordings was either set to 300 s (7 fps), or 120 s (10 fps). We chose these values to allow for droplet trajectory reconstruction. The size of the observation window is $\sim 5 \text{ mm} \times 2 \text{ mm}$, representing approximately $\sim 10\%$ of the cell, in which we ensure that the density field is relatively homogeneous. Each experiment was conducted with a fixed magnetic field, which was then increased in increments of 0.364 mT until reaching its maximum value of 10 mT.

C.2. Particle Detection & Tracking. To detect the drop position, we find the local intensity maxima in each image. To detect all the particles, the following pre-processing steps were applied: the image contrast is automatically increased and a Gaussian blur with a size of 2.5 px applied to smooth the intensity profile. This provides a list of coordinates for each particle and for each frame (see Figure S3A). We track the particles and reconstruct their trajectories using the Crocker and Grier method (5). We show typical trajectories in Figure S3B. We compute the Delaunay triangulation diagram and the adjacency matrix based on the particle positions in each frame. This allows to associate each particle to its nearest neighbors.

C.3. Translational and orientational order parameter. We define two order parameters.

- **Translational order.** $g(\mathbf{r})$ quantifies the degree of correlation between the particle positions. It is defined as the probability (per unit volume) to find a particle at the position $\mathbf{r} + \mathbf{R}$ given a particle at \mathbf{R} : $g(\mathbf{r}) = \frac{1}{\langle n \rangle} \left\langle \sum_{j \neq i}^N \delta(\mathbf{r}_i - \mathbf{r}_j) \right\rangle_i$, where $\langle n \rangle$ is the average number density.
- **Oriental order.** The hexatic order parameter ψ_6 quantifies how close to a hexagonal arrangement the nearest neighbour of a particle are. We compute it as $\psi_6(\mathbf{r}_i) = \frac{1}{N_i} \sum_{j=0}^{N_i} e^{6i\theta_{ij}}$ with θ_{ij} the angle between the N_i nearest neighbors. $\psi_6(\mathbf{r}_i)$ is a complex number, we define its modulus $|\psi_6|$ and argument $\theta_6 = \frac{1}{6} \arg[\psi_6(\mathbf{r}_i)]$.

C.4. Power spectra & Dispersion relations.

Hexatic order parameter waves To define a hexatic order parameter field $\psi_6(\mathbf{r}, t)$ (and $\theta_6(\mathbf{r}, t)$), we interpolate the value of ψ_6 evaluated in each Voronoï cell on a square lattice, see Figure S3C. The spectral power density of the Eulerian fields $f(\mathbf{r}, t) = \psi_6(\mathbf{r}, t) - \overline{\psi_6}$ is given by

$$\mathcal{P}_6(\mathbf{q}, \omega) = |\tilde{f}(\mathbf{q}, \omega)|^2 \quad [1]$$

where, $\overline{\psi_6}$ is the space and time average of the hexatic order parameter, and $\tilde{f}(\mathbf{q}, \omega)$ is the spatio-temporal Fourier transform of $f(\mathbf{r}, t)$ in the laboratory frame. In practice, we compute this spectrum using the Matlab algorithm for three-dimensional fast Fourier transform. We note that we keep only the values above the crystalline threshold (namely $\psi_6 > 0.65$) to compute all spectra, values below this threshold are set to 0. In all the experiments, the typical resolutions are $\delta q = 6.10^{-4} \mu\text{m}^{-1}$ in the spacial domain, and $\delta\omega = 0.05 \text{ s}^{-1}$ in the temporal domain.

We outline the procedure for extracting the dispersion relation from the raw power spectra of ψ_6 . First, we reduce the Fourier space to two dimensions by considering only wave-vectors in the direction of the mean flow ($q_y = 0$). Next, we transition to the comoving frame by applying a linear transformation $M = \begin{pmatrix} 1 & 0 \\ -U & 1 \end{pmatrix}$ to the spectrum such that $\omega'(q_x) = \omega(q_x) - Uq_x$. The transformed image is then linearly interpolated onto a rectangular grid and smoothed for each frequency using a moving average. Finally, the dispersion relation is extracted by identifying the maximum value of the spectrum at each frequency for every wave-vector.

2. Propagation of density waves and dipolar hydrodynamic interactions

In this section we provide additional evidence that the hydrodynamic couplings between the driven droplets are well captured by the standard dipolar interactions extensively studied in e.g. (6–9). Driven isotropic emulsions have been consistently shown to support sound waves despite the overdamped dynamics of all the individual particles (6, 7). The dispersion relation of the sound waves provides a direct insight into the range and symmetry of the underlying hydrodynamic interactions. Following the same method as for the hexatic order parameter (see Eq. (1) and Figure 3A in the main text), we compute the fluctuation spectrum of the density fluctuations

$$\mathcal{P}_\rho(\mathbf{q}, \omega) = |\tilde{\rho}(\mathbf{q}, \omega)|^2, \quad [2]$$

where $\tilde{\rho}(\mathbf{q}, \omega)$ is the Fourier spectrum of the number density field $\rho(\mathbf{r}, t)$. In Figure S2A, we plot the power spectra evaluated at $q_y = 0$ for different values of the B field. In agreement with earlier results, we find that the spectra are peaked on a nontrivial curve in the (q_x, ω) plane, which reveals the propagation of sound modes. Increasing the value of B , not surprisingly, we find that the density waves are progressively suppressed. Ultimately, we observe a simple dynamics where the density field hardly fluctuates, and is merely advected at the mean crystal speed. The lively dynamics of the domain walls discussed in the main text does not translate in strong density fluctuations.

Locating the maxima of \mathcal{P}_ρ , and repeating the same measurement for all values of q_y , we can construct the dispersion relation $\omega = f(q_x, q_y)$ showed in Figure S2B. In the liquid phase where no crystalline order prevails, the dispersion relations are identical to that reported in Eq. 6 in (7). In Figure S2C, we compare our measurements to the theory of (7). We find that over a range of B fields, in the melted regime, the dispersion relation of the density waves are quantitatively captured by our model where the only interactions between the droplets are hydrodynamic dipoles and steric repulsion. This agreement confirms the relevance of the dipolar interactions to account for the dynamics observed in our experiments.

3. Robustness of our experimental results to changes in the area fraction

As alluded to in the main text we have conducted a second series of experiments where the packing fraction is $\phi = 0.61$, for droplets having a slightly different radius $a = 47 \mu\text{m}$. None of our main findings are qualitatively different from that reported in the main text. Figure S4 reports the evolution of the translational and orientational order parameters as B is varied. All our measurements confirm the robustness of the melting scenario. Under the action of non-reciprocal forces, crystals melts from their grain boundaries whose the size continuously shrink as B decreases. Of course as the packing fraction increases, the contact interactions play a more significant role and stabilizes the crystal phase. Even when the B field is vanishingly small, the contact interactions stabilizes the ordering of minute crystallites.

4. Driven emulsion crystal: Model and numerical simulations

A. Model. We detail the minimal model introduced in the main text. We consider a collection of N particles that evolves according to an overdamped dynamics under the action of pairwise-additive interactions that depend only on the (vector) distance between droplets. The position \mathbf{R}_i of a the i^{th} droplet evolves in time as

$$\zeta \dot{\mathbf{R}}_i = \sum_{j \neq i} \mathbf{F}(\mathbf{R}_i - \mathbf{R}_j), \quad [3]$$

where ζ is a friction coefficient. The forces decompose as

$$\mathbf{F}(\mathbf{r}) = \mathbf{F}_{\text{core}}(\mathbf{r}) + \mathbf{F}_{\text{mag}}(\mathbf{r}) + \mathbf{F}_{\text{hydro}}(\mathbf{r}), \quad [4]$$

with \mathbf{F}_{core} , \mathbf{F}_{mag} and $\mathbf{F}_{\text{hydro}}$ being respectively the hard-core, magnetic and hydrodynamic forces. We detail them below. Note that any advection term at velocity \mathbf{V}_0 in Eq. (3) could be eliminated by a change of coordinates $\mathbf{r} \mapsto \mathbf{r} - \mathbf{V}_0 t$. The mean advection plays no role in our modeling and simulations we ignore it in all that follows.

Hard-core repulsion. The droplets cannot interpenetrate one another. We implement this constraint with a strongly repulsive potential Weeks-Chandler-Andersen (WCA) potential

$$\phi_{\text{WCA}}(r) = \begin{cases} 4\tilde{\epsilon} \left[\left(\frac{r_0}{r} \right)^{12} - \left(\frac{r_0}{r} \right)^6 \right] + \tilde{\epsilon} & \text{if } r \leq 2^{1/6} r_0 \\ 0 & \text{otherwise} \end{cases}, \quad [5]$$

with $r_0 = 2\tilde{a}/2^{1/6}$ with \tilde{a} the radius of the droplets. The resulting repulsion force is simply given by $\mathbf{F}_{\text{core}}(\mathbf{r}) = -\nabla \phi_{\text{WCA}}(\mathbf{r})$.

Magnetic interactions. In the presence of an external magnetic field, the droplets behave as magnetic dipoles pointing in the z direction and repel one another with a repulsive dipole-dipole potential

$$\phi_{\text{mag}}(r) = \frac{\tilde{B}}{r^3}. \quad [6]$$

The magnetic force is $\mathbf{F}_{\text{mag}}(\mathbf{r}) = -\nabla \phi_{\text{mag}}(\mathbf{r})$. In the experiments $\tilde{B} = \frac{\mu_0(1+\chi)m^2}{4\pi}$ with $m = \frac{\chi v B}{\mu_0}$ the magnetic moment of a droplet of volume v , χ the magnetic susceptibility and m the magnetic dipole strength. We are not interested in the long-range effects of the magnetic interactions: in the numerical simulations, a cut-off is introduced at a distance corresponding to half the box height.

Hydrodynamic interactions. In a Hele-Shaw cell, the 2D velocity field $\mathbf{u}(\mathbf{r})$ of a viscous fluid obeys Darcy's law $\mathbf{u}(\mathbf{r}) = -\kappa \nabla P(\mathbf{r})$ with $P(\mathbf{r})$ the pressure field and κ the permeability of the channel. The fluid is incompressible, the continuity equations then reduces to $\nabla \cdot \mathbf{u} = 0$. When an intruder, e.g. a squeezed droplet, moves at a velocity different from the fluid's, it induces long range perturbations on the flow. In the far field limit the flow perturbation induced by an finite-size intruder at the origin is well approximated as a source dipole singularity: $\nabla \cdot \mathbf{u} = -\tilde{\sigma} \cdot \nabla \delta(\mathbf{r})$ with $\delta(\mathbf{r})$ the Dirac function. The dipole strength $\tilde{\sigma}$ can be expressed in terms of the area of the intruder and the velocity difference. This modeling can be understood as follows. To allow the intruder to move some fluid matter must be removed downstream and injected upstream hence forming a source dipole. If another particle is placed at position \mathbf{R} inside this flow perturbation, it is advected at a velocity $\zeta^{-1} \mathbf{F}_{\text{hydro}}(\mathbf{R}) = \mu \mathbf{u}(\mathbf{R})$ where μ is the dimensionless mobility of the particle, see e.g. Ref. (7) for more details. Lastly, the hydrodynamic force between two droplets satisfies the equations

$$\mathbf{F}_{\text{hydro}}(\mathbf{r}) = -\nabla \phi_{\text{hydro}}(\mathbf{r}) \quad [7]$$

$$\nabla \cdot \mathbf{F}_{\text{hydro}}(\mathbf{r}) = -\tilde{\sigma} \cdot \nabla \delta(\mathbf{r}), \quad [8]$$

where ϕ_{hydro} is the hydrodynamic potential proportional to P , and $\tilde{\sigma}$ is a dipole strength proportional to $\tilde{\sigma}$. Together, these two equations imply that ϕ_{hydro} obeys a Poisson equation,

$$\nabla^2 \phi_{\text{hydro}}(\mathbf{r}) = q(\mathbf{r}) \quad [9]$$

with $q(\mathbf{r}) = \tilde{\sigma} \cdot \nabla \delta(\mathbf{r})$. The Poisson equation is easily solved from the Green function of the 2D Laplacian:

$$\phi_{\text{hydro}}(\mathbf{r}) = \tilde{\sigma} \cdot \nabla \left(\frac{1}{2\pi} \ln r \right) = \frac{1}{2\pi} \frac{\tilde{\sigma} \cdot \mathbf{r}}{r^2}. \quad [10]$$

We stress that the hydrodynamic potential has the unusual symmetry $\nabla \phi_{\text{hydro}}(-\mathbf{r}) = -\nabla \phi_{\text{hydro}}(\mathbf{r})$ which induces forces that do not obeys the action-reaction principle as $\mathbf{F}_{\text{hydro}}(-\mathbf{r}) = \mathbf{F}_{\text{hydro}}(\mathbf{r})$. The hydrodynamic interactions are non-reciprocal.

B. Dimensionless parameters. Considering Eq. (3), we have six parameters and three units: energy $[E]$, length $[L]$ and time $[T]$. This enables us to set three parameters to unity in the numerical simulations, or alternatively to construct three dimensionless numbers. The six dimensional parameters are: the number density ρ (number of particles per surface area) with unit $[L^{-2}]$, the particle diameter \tilde{a} with unit $[L]$, the strength of the WCA potential $\tilde{\epsilon}$ with unit $[E]$, the magnetic strength \tilde{A} with unit $[EL^3]$, the hydrodynamic dipole σ with unit $[EL]$ and the friction coefficient ζ with unit $[EL^{-2}T]$. Let us deal successively with length, energy and time scales.

- We set $\rho = 1$: the typical length scale is set to $\ell^* = \rho^{-1/2}$. This gives us a first dimensionless number as the scaled particle radius $a = \rho^{1/2}\tilde{a}$, or alternatively the packing fraction $\phi = \pi\rho\tilde{a}^2 = \pi a^2$.
- We set $\sigma = 1$: the typical energy scale is set to $E^* = \rho^{1/2}\sigma$. This gives us two dimensionless numbers: the crucial ratio between magnetic and hydrodynamic forces $\mathcal{B} = \rho\mathcal{B}/\sigma$, and the scaled WCA strength $\epsilon = \rho^{1/2}\tilde{\epsilon}/\sigma$.
- We set $\zeta = 1$: the timescale of the simulations is $t^* = \zeta/[\rho^{3/2}\sigma]$.

At the end of day, the three dimensionless parameters are: the packing fraction ϕ , the magnetic to hydrodynamic ratio \mathcal{B} and the scaled WCA strength ϵ . The most important one is A and we study systematically its influence on the system. As for the packing fraction, we provide data for two values: dilute system $\phi = 0.36$ ($a = 0.34$) and dense system $\phi = 0.61$ ($a = 0.44$). The strength of the WCA interactions is not expected to play any role in the physics of the system and we set $\epsilon = 1$ in all the simulations.

C. Details of the numerical simulations. The simulations are performed in a periodic box of size $L_x \times L_y$. N particles are placed in this box, so that the density $\rho = N/(L_x L_y) = 1$. Simulations snapshots correspond to $L_x = 128$, $L_y = 64$ and $N = 8192$; and averaged observables to $L_x = L_y = 64$ and $N = 4096$. The particles are initially placed at random and harmonic repulsive interactions are implemented to relax the system to a state where particles do not overlap (that is to say, they are at a distance larger than $2a$).

Starting from this initial condition, the forces $\mathbf{F}_i(t)$ at a given time t are computed as detailed below, and the positions $\mathbf{R}_i(t)$ are updated according to an explicit Euler scheme: $\mathbf{R}_i(t + \Delta t) = \mathbf{R}_i(t) + \Delta t \mathbf{F}_i(t)$. We used a timestep $\Delta t = 0.002$ and perform up to $6 \cdot 10^6$ iterations (final time $t_{\max} = 1200$). The first $2 \cdot 10^6$ iterations ($t = 400$) lead the system to its steady state, and the observables related to this steady state are computed by averaging over the $4 \cdot 10^6$ remaining iterations.

The forces are computed as follow. The WCA interactions involve only particles touching one another. The magnetic interactions (that decay as $1/r^3$) are cut-off at a distance $L_y/2$. And the long-range hydrodynamic interactions are carefully implemented using a modified Ewald algorithm (10) which we introduce below.

D. Ewald algorithm for the hydrodynamic forces. We consider N dipoles σ at positions \mathbf{R}_i in a periodic box of size (L_x, L_y) . We call \mathbf{S} the lattice vectors corresponding to this periodic box ($S_x = \frac{2\pi}{L_x}n_x$, $S_y = \frac{2\pi}{L_y}n_y$ with integers n_x and n_y). The charge density that satisfies the Poisson equation Eq. (9) is

$$q(\mathbf{r}) = \sum_{i=1}^N \sum_{\mathbf{S}} \sigma \cdot \nabla \delta(\mathbf{r} - (\mathbf{R}_i + \mathbf{S})). \quad [11]$$

The solution is

$$\phi(\mathbf{r}) = \frac{1}{2\pi} \sum_{i=1}^N \sum_{\mathbf{S}} \frac{\sigma \cdot (\mathbf{r} - (\mathbf{R}_i + \mathbf{S}))}{(\mathbf{r} - (\mathbf{R}_i + \mathbf{S}))^2}. \quad [12]$$

In this section, we remove the subscript ‘hydro’ for the sake of clarity. The hydrodynamic force acting on particle i is $\mathbf{F}_i = -\nabla\phi(\mathbf{R}_i)$:

$$\mathbf{F}_i = \frac{1}{2\pi} \sum_{(j,\mathbf{S}) \neq (i,0)} \left[\frac{2\hat{\mathbf{R}}_{i,j,\mathbf{S}}\hat{\mathbf{R}}_{i,j,\mathbf{S}} - 1}{\mathbf{R}_{i,j,\mathbf{S}}^2} \right] \cdot \sigma, \quad [13]$$

with $\mathbf{R}_{i,j,\mathbf{S}} = \mathbf{R}_i - \mathbf{R}_j - \mathbf{S}$, $\hat{\mathbf{R}}_{i,j,\mathbf{S}} = \mathbf{R}_{i,j,\mathbf{S}}/|\mathbf{R}_{i,j,\mathbf{S}}|$ and the term with both $j = i$ and $\mathbf{S} = 0$ is excluded from the sum.

The direct summation converges very slowly and is unfit for numerical simulations. We therefore adapt the Ewald summation (10), initially developed for electric charges and reciprocal electric interactions.

Decomposition. We decompose the density into a screened part, that we compute in real space, and a Gaussian part, that we compute in Fourier space:

$$q(\mathbf{r}) = q_R(\mathbf{r}) + q_F(\mathbf{r}) \quad [14]$$

with

$$q_R(\mathbf{r}) = \sum_{i=1}^N \sum_{\mathbf{S}} \sigma \cdot \nabla \left[\delta(\mathbf{r} - (\mathbf{R}_i + \mathbf{S})) - \frac{\alpha^2}{\pi} e^{-\alpha^2(\mathbf{r} - (\mathbf{R}_i + \mathbf{S}))^2} \right], \quad [15]$$

$$q_F(\mathbf{r}) = \sum_{i=1}^N \sum_{\mathbf{S}} \sigma \cdot \nabla \left[\frac{\alpha^2}{\pi} e^{-\alpha^2(\mathbf{r} - (\mathbf{R}_i + \mathbf{S}))^2} \right]. \quad [16]$$

The parameter α is free and is adjusted to obtain the fastest computation. We now detail how we compute the Fourier-space, and the real-space components of the hydrodynamic forces.

Fourier space component. We move to Fourier space (\mathbf{G} : vector in reciprocal space, $|\mathcal{V}|$: volume of the unit cell) and decompose q_F into a Fourier series

$$q_F(\mathbf{r}) = \frac{1}{|\mathcal{V}|} \sum_{\mathbf{G}} e^{i\mathbf{G} \cdot \mathbf{r}} \tilde{q}_F(\mathbf{G}). \quad [17]$$

Using $\nabla \phi_F(\mathbf{r}) = q_F(\mathbf{r})$, the computation leads to

$$\tilde{q}_F(\mathbf{G}) = \int_{\mathcal{V}} d\mathbf{r} e^{-i\mathbf{k} \cdot \mathbf{G}} q_F(\mathbf{r}) = \int_{\mathbb{R}^2} d\mathbf{r} e^{-i\mathbf{k} \cdot \mathbf{G}} \sum_{i=1}^N \boldsymbol{\sigma} \cdot \nabla \left[\frac{\alpha^2}{\pi} e^{-\alpha^2(\mathbf{r}-\mathbf{R}_i)^2} \right] = (i\mathbf{G} \cdot \boldsymbol{\sigma}) e^{-\frac{\mathbf{G}^2}{4\alpha^2}} \sum_{j=1}^N e^{-\mathbf{G} \cdot \mathbf{R}_j} \quad [18]$$

$$\tilde{\phi}_F(\mathbf{G}) = -\frac{1}{\mathbf{G}^2} (i\mathbf{G} \cdot \boldsymbol{\sigma}) e^{-\frac{\mathbf{G}^2}{4\alpha^2}} \sum_{j=1}^N e^{-\mathbf{G} \cdot \mathbf{R}_j}. \quad [19]$$

The real-space expression of the potential, assuming its average vanishes, is

$$\phi_F(\mathbf{r}) = \frac{1}{|\mathcal{V}|} \sum_{\mathbf{G}} e^{i\mathbf{G} \cdot \mathbf{r}} \tilde{\phi}_F(\mathbf{G}) = \frac{1}{|\mathcal{V}|} \sum_{\mathbf{G} \neq 0} \frac{-i\mathbf{G} \cdot \boldsymbol{\sigma}}{\mathbf{G}^2} e^{-\frac{\mathbf{G}^2}{4\alpha^2}} \sum_{j=1}^N e^{i\mathbf{G} \cdot (\mathbf{r}-\mathbf{R}_j)} \quad [20]$$

$$= \frac{1}{|\mathcal{V}|} \sum_{\mathbf{G} \neq 0} \frac{\mathbf{G} \cdot \boldsymbol{\sigma}}{\mathbf{G}^2} e^{-\frac{\mathbf{G}^2}{4\alpha^2}} \sum_{j=1}^N \sin[\mathbf{G} \cdot (\mathbf{r} - \mathbf{R}_j)] \quad [21]$$

And the force on particle i , $\mathbf{F}_{F,i} = -\nabla \phi_F(\mathbf{R}_i)$ excluding the term $j = i$, is

$$\mathbf{F}_{F,i} = \frac{-1}{|\mathcal{V}|} \left\{ (N-1) \frac{\boldsymbol{\sigma}}{2} + \sum_{\mathbf{G} \neq 0} \left(\sum_{j \neq i} \cos[\mathbf{G} \cdot (\mathbf{R}_i - \mathbf{R}_j)] \right) e^{-\frac{\mathbf{G}^2}{4\alpha^2}} \frac{(\mathbf{G} \cdot \boldsymbol{\sigma}) \mathbf{G}}{\mathbf{G}^2} \right\}. \quad [22]$$

This sum converges exponentially fast. One subtlety is that there is a component for 0 wave-number. It comes from the relation $\frac{(\mathbf{k} \cdot \boldsymbol{\sigma}) \mathbf{k}}{\mathbf{k}^2} \sim \frac{\boldsymbol{\sigma}}{2}$ as $\mathbf{k} \rightarrow \mathbf{0}$ “in a isotropic way” that can be obtained by inverting the Fourier transform and computing the integral over space with integration first perform over the angular coordinate.

Another important remark is that the sum over j can be computed from the structure factor $S(\mathbf{G})$,

$$\sum_{j \neq i} \cos[\mathbf{G} \cdot (\mathbf{R}_i - \mathbf{R}_j)] = \text{Re}[S(\mathbf{G})] \cos(\mathbf{G} \cdot \mathbf{R}_i) + \text{Im}[S(\mathbf{G})] \sin(\mathbf{G} \cdot \mathbf{R}_i) - 1, \quad [23]$$

$$S(\mathbf{G}) = \sum_j e^{i\mathbf{G} \cdot \mathbf{R}_j}. \quad [24]$$

The computation of the N forces is therefore done in linear time and not in quadratic time, and the constant factors can be precomputed.

Real space component. To compute the real-space contribution, we first investigate the case of a single particle in infinite space,

$$q_R^{(1)}(\mathbf{r}) = \boldsymbol{\sigma} \cdot \nabla \left[\delta(\mathbf{r}) - \frac{\alpha^2}{\pi} e^{-\alpha^2 \mathbf{r}^2} \right], \quad [25]$$

$$\tilde{q}_R^{(1)}(\mathbf{k}) = i\mathbf{k} \cdot \boldsymbol{\sigma} \left[1 - e^{-\frac{\mathbf{k}^2}{4\alpha^2}} \right], \quad [26]$$

$$\tilde{\phi}_R^{(1)}(\mathbf{k}) = \frac{-i\mathbf{k} \cdot \boldsymbol{\sigma}}{\mathbf{k}^2} \left[1 - e^{-\frac{\mathbf{k}^2}{4\alpha^2}} \right]. \quad [27]$$

Inverting the Fourier transform leads to

$$\phi_R^{(1)}(\mathbf{r}) = \frac{-i\boldsymbol{\sigma}}{(2\pi)^2} \int_0^\infty dk \left(1 - e^{-\frac{k^2}{4\alpha^2}} \right) \int_0^{2\pi} d\varphi e^{ikr \cos(\varphi-\theta)} \cos(\varphi-\alpha) = \frac{\boldsymbol{\sigma} \cdot \hat{\mathbf{r}}}{2\pi r} e^{-\alpha^2 \mathbf{r}^2}, \quad [28]$$

$$-\nabla \phi_R^{(1)}(\mathbf{r}) = \frac{e^{-\alpha^2 \mathbf{r}^2}}{2\pi} \left[\frac{2(\boldsymbol{\sigma} \cdot \hat{\mathbf{r}}) \hat{\mathbf{r}} - \boldsymbol{\sigma}}{\mathbf{r}^2} + 2\alpha^2 (\boldsymbol{\sigma} \cdot \hat{\mathbf{r}}) \hat{\mathbf{r}} \right], \quad [29]$$

with $\hat{\mathbf{r}} = \mathbf{r}/r$. We can now sum all the contributions and obtain

$$\phi_R(\mathbf{r}) = \frac{1}{2\pi} \sum_{i=1}^N \sum_{\mathbf{S}} \frac{\boldsymbol{\sigma} \cdot (\mathbf{r} - \mathbf{R}_i - \mathbf{S})}{(\mathbf{r} - \mathbf{R}_i - \mathbf{S})^2} e^{-\alpha(\mathbf{r} - \mathbf{R}_i - \mathbf{S})^2}, \quad [30]$$

$$\mathbf{F}_{R,i} = \sum_{j \neq i} \sum_{\mathbf{S}} \frac{e^{-\alpha^2 \mathbf{R}_{i,j,\mathbf{S}}^2}}{2\pi} \left[\frac{2\hat{\mathbf{R}}_{i,j,\mathbf{S}} \hat{\mathbf{R}}_{i,j,\mathbf{S}} - 1}{\mathbf{R}_{i,j,\mathbf{S}}^2} + 2\alpha^2 \hat{\mathbf{R}}_{i,j,\mathbf{S}} \hat{\mathbf{R}}_{i,j,\mathbf{S}} \right] \cdot \boldsymbol{\sigma}. \quad [31]$$

The sum converges exponentially fast.

Self-interaction. In Eq. (22) and Eq. (31), we excluded the term $j = i$ from the summation as a droplet is not advected by its own flow. However, in periodic space a droplet does interact with its images. This is irrelevant for reciprocal forces ($\mathbf{F}(-\mathbf{r}) = -\mathbf{F}(\mathbf{r})$) since the contributions from the images compensate. But in our non-reciprocal case ($\mathbf{F}(-\mathbf{r}) = \mathbf{F}(\mathbf{r})$), the interaction of a droplet with its images, that we call “self-interaction”, can be non-zero. The self-interaction force \mathbf{F}_{self} is the same for all particles and reads

$$\mathbf{F}_{\text{self}} = \frac{1}{2\pi} \sum_{\mathbf{S} \neq 0} \left[\frac{2\hat{\mathbf{S}}\hat{\mathbf{S}} - 1}{\mathbf{S}^2} \right] \cdot \boldsymbol{\sigma}, \quad [32]$$

where the sum is on non-zero reciprocal space vector and $\hat{\mathbf{S}} = \mathbf{S}/|\mathbf{S}|$. This sum is not absolutely convergent: we consider the limit corresponding to a summation over the same number of boxes in the x and y directions.

Summary. At the end of the day, the slowly converging sum from Eq. (13), is replaced by

$$\mathbf{F}_i = \mathbf{F}_{f,i} + \mathbf{F}_{r,i} + \mathbf{F}_{\text{self}}, \quad [33]$$

with $\mathbf{F}_{r,f}$ given by Eq. (22) which converges exponentially fast in Fourier space, $\mathbf{F}_{r,i}$ given by Eq. (31) which converges exponentially fast in real space, and \mathbf{F}_{self} given by Eq. (32) that is computed only once. The parameter α is free and is optimized such that the trade-off between computations in Fourier and real spaces is as fast as possible.

5. Non-reciprocal interactions propel dislocations

In this section we generalize the results presented in (11). Both in our experiments and numerical simulations, we observe that the crystal defects propel in the upstream direction, see Fig. 3. We explain our observations based on kinematics and symmetry arguments in the discussion section of the main text. Here, we provide a more technical and accurate explanation for the propulsion of dislocations powered by non-reciprocal interactions. This section is organized as follows: (i) we discuss the stability of crystals challenged by non-reciprocal forces. In particular, we show that hydrodynamic interaction arising from Darcy’s flows cannot lead to a linear instability of driven crystals. (ii) We provide a general expression for \mathbf{F}^{NR} in the case of short-ranged non-reciprocal interactions, and discuss its relation to the early model introduced in (12). (iii) We focus on the long-range hydrodynamic interactions relevant to our experiments, we compute \mathbf{F}^{NR} and \mathbf{u}^{NR} . (iv) We put our results in the context of the Peach-Koehler force formalism (13). (v) We explain how dislocations glide and split in response to \mathbf{F}^{NR} . (vi) Lastly, we discuss the impact of our results on the dynamics of grain-boundaries.

A. Can non-reciprocal forces destabilize driven lattices?.

A.1. General case and potential flows. For the sake of clarity, unlike in Section 4 and Eq. 1 in the main text, we consider here the overdamped dynamics of a hexagonal lattice of particles interacting only via non-reciprocal forces:

$$\zeta \partial_t \mathbf{R}_i = \sum_{j \neq i} \mathbf{F}(\mathbf{R}_i - \mathbf{R}_j), \quad [34]$$

and by definition $\mathbf{F}(-\mathbf{r}) = \mathbf{F}(\mathbf{r})$. For instance \mathbf{F} can represent $\mathbf{F}_{\text{hydro}}$ introduced in Eq. 1 in the main text. However, we henceforth keep the discussion more general and specify the form and origin of the non-reciprocal force only when needed.

To study the stability of the arrangement of particles, we define the displacement field $\mathbf{u}(\mathbf{r})$ and its Fourier transform $\tilde{\mathbf{u}}(\mathbf{q})$. The conventions are

$$\tilde{\mathbf{u}}(\mathbf{q}) = \int d\mathbf{r} e^{-i\mathbf{q} \cdot \mathbf{r}} \mathbf{u}(\mathbf{r}), \quad \mathbf{u}(\mathbf{r}) = \frac{1}{(2\pi)^2} \int d\mathbf{q} e^{+i\mathbf{q} \cdot \mathbf{r}} \tilde{\mathbf{u}}(\mathbf{q}). \quad [35]$$

The resulting linear dynamics is then defined by the stability matrix $M(\mathbf{q})$ as

$$\zeta \partial_t \tilde{\mathbf{u}}(\mathbf{q}) = M(\mathbf{q}) \cdot \tilde{\mathbf{u}}(\mathbf{q}) \quad [36]$$

$$M(\mathbf{q}) = i \sum_{j \neq 0} \sin(\mathbf{q} \cdot \mathbf{r}_j) \nabla \mathbf{F}(\mathbf{r}_j) \quad [37]$$

where \mathbf{r}_j (norm r_j and angle θ_j) are the positions of the particles, see (11). We used the fact that $\mathbf{F}(-\mathbf{r}) = \mathbf{F}(\mathbf{r})$. We note that the inverse Fourier transform of the right-hand side of Eq. (36) is the non-reciprocal force field \mathbf{F}^{NR} . As discussed in (11), without additional constraints on \mathbf{F} , the dynamics is either marginally stable or unstable. However when the non-reciprocal forces arise from 2D potential fluid flows, such as viscous Darcy's flows, \mathbf{F} enjoys an additional property. \mathbf{F} can be either written in term of a potential $\mathbf{F} = \nabla\phi$, or a stream function $\mathbf{F} = \nabla^\perp\psi$, so that:

$$\nabla\mathbf{F} = \begin{pmatrix} \frac{\partial F_x}{\partial x} & \frac{\partial F_x}{\partial y} \\ \frac{\partial F_y}{\partial x} & \frac{\partial F_y}{\partial y} \end{pmatrix} = \begin{pmatrix} \frac{\partial^2 \psi}{\partial x \partial y} & \frac{\partial^2 \phi}{\partial x \partial y} \\ \frac{\partial^2 \phi}{\partial x \partial y} & -\frac{\partial^2 \psi}{\partial x \partial y} \end{pmatrix} \quad [38]$$

The sum in Eq. (37) leads to a matrix of the form

$$M(\mathbf{q}) = i \begin{pmatrix} m_1 & m_2 \\ m_2 & -m_1 \end{pmatrix} \quad [39]$$

where m_1 and m_2 are real numbers. The eigenvalues are $\pm i\sqrt{m_1^2 + m_2^2}$ and the system is therefore marginally stable.

A.2. 2D lattices hydrodynamically driven through viscous fluids are marginally stable. In the specific case of dipolar hydrodynamic interactions, $\phi(\mathbf{r}) = \sigma \cos \theta/r$, and $\psi(\mathbf{r}) = -\sigma \sin \theta/r$. The nonreciprocal hydrodynamic force takes the form

$$\mathbf{F}(\mathbf{r}) = \frac{-\sigma}{r^2} \begin{pmatrix} \cos(2\theta) \\ \sin(2\theta) \end{pmatrix}, \quad [40]$$

Note that, to simplify the algebra, our notation of the strength σ of the dipolar force differs from that used in Section 4.

The associated Jacobian matrix reads

$$\nabla\mathbf{F}(\mathbf{r}) = \frac{2\sigma}{r^3} \begin{pmatrix} \cos(3\theta) & \sin(3\theta) \\ \sin(3\theta) & -\cos(3\theta) \end{pmatrix}, \quad [41]$$

and the stability matrix is given by

$$M(\mathbf{q}) = 2i\sigma \sum_{j \neq 0} \frac{\sin(qr \cos(\theta_j - \varphi))}{r_j^3} \begin{pmatrix} \cos(3\theta_j) & \sin(3\theta_j) \\ \sin(3\theta_j) & -\cos(3\theta_j) \end{pmatrix} \quad [42]$$

We can compute the sum Eq. (42) numerically for an hexagonal crystal having the shape of a circle of radius R and a unit lattice spacing ($\sigma = 1$). In limit of infinitely large systems ($qR \gg 1$), we find

$$m_1 \approx -1.8q \cos(3\varphi), \quad m_2 \approx -1.8q \sin(3\varphi), \quad [43]$$

independently of the orientation of the crystal, where φ is the angle of the wavevector \mathbf{q} . To make sense of this scaling, we can approximate the sum Eq. (37) by its continuum equivalent assuming a homogeneous density $\bar{\rho} = 2/(a^2\sqrt{3})$, where a is the lattice spacing. This leads to

$$m_1 = 2\sigma\bar{\rho} \int_0^\infty dr r \int_0^{2\pi} d\theta \frac{\sin(qr \cos(\theta - \varphi))}{r^3} \cos(3\theta) = -\frac{\pi\sigma\bar{\rho}}{2} q \cos(3\varphi), \quad [44]$$

$$m_2 = 2\sigma\bar{\rho} \int_0^\infty dr r \int_0^{2\pi} d\theta \frac{\sin(qr \cos(\theta - \varphi))}{r^3} \sin(3\theta) = -\frac{\pi\sigma\bar{\rho}}{2} q \sin(3\varphi). \quad [45]$$

We note that $\frac{\pi\bar{\rho}}{2} = \frac{\pi}{\sqrt{3}} = 1.81$ in quantitative agreement with the numerical summation ($a = 1$). This result is consistent with the earlier predictions of (7, 9): driven hydrodynamic crystals are marginally stable. It is worth noting that the addition of elastic forces can only further stabilize the crystal dynamics, see e.g. (14) for a comprehensive discussion.

B. Short-range nonreciprocal interactions.

B.1. Computation of \mathbf{F}^{NR} . When the nonreciprocal forces \mathbf{F} are short ranged (we note ℓ their typical range), we can take the long wavelength limit $q\ell \ll 1$ in Eq. (37), which yields

$$M(\mathbf{q}) \underset{q\ell \ll 1}{\sim} \sum_{j \neq 0} (i\mathbf{q} \cdot \mathbf{r}_j) \nabla\mathbf{F}(\mathbf{r}_j). \quad [46]$$

This relation allows us to express \mathbf{F}^{NR} as a gradient expansion:

$$F_\alpha^{\text{NR}} = A_{\alpha\beta\gamma} \partial_\gamma u_\beta \quad [47]$$

where

$$A_{\alpha\beta\gamma} = \sum_j r_{j,\beta} \partial_\gamma F_\alpha(\mathbf{r}_j). \quad [48]$$

The above tensor depends on the symmetries of both the crystal structure and of the force \mathbf{F} .

To illustrate the above calculation on a specific example, we consider short range interactions having the same dipolar symmetry as the hydrodynamic dipoles:

$$\mathbf{F}(\mathbf{r}) = f(r) \begin{pmatrix} \cos(2\theta) \\ \sin(2\theta) \end{pmatrix}, \quad [49]$$

$$\nabla \mathbf{F}(\mathbf{r}) = \begin{pmatrix} \cos \theta \left[\cos(2\theta) f'(r) + 4 \sin^2 \theta \frac{f(r)}{r} \right] & \sin \theta \left[\cos(2\theta) f'(r) - 4 \cos^2 \theta \frac{f(r)}{r} \right] \\ \cos \theta \sin(2\theta) f'(r) - 2 \cos(2\theta) \sin \theta \frac{f(r)}{r} & \sin(2\theta) \sin \theta f'(r) + 2 \cos(2\theta) \cos \theta \frac{f(r)}{r} \end{pmatrix}. \quad [50]$$

For instance $f(r) = -e^{-r/\ell}$. Using the six-fold symmetry of the lattice in Eq. (46) we find

$$M(\mathbf{q}) \underset{qb \ll 1}{\sim} K \begin{pmatrix} iq \cos \varphi & -iq \sin \varphi \\ iq \sin \varphi & iq \cos \varphi \end{pmatrix} = K \begin{pmatrix} iq_x & -iq_y \\ iq_y & iq_x \end{pmatrix}, \quad [51]$$

$$K = \frac{1}{4} \sum_j [2f(r_j) + r_j f'(r_j)]. \quad [52]$$

In other words we can express \mathbf{F}^{NR} as

$$\mathbf{F}^{\text{NR}} = K \begin{pmatrix} \frac{\partial u_x}{\partial x} - \frac{\partial u_y}{\partial y} \\ \frac{\partial u_x}{\partial y} + \frac{\partial u_y}{\partial x} \end{pmatrix} \quad [53]$$

Two comments are in order. Firstly changing the range of the dipolar interactions has a strong impact on the stability of the crystal. The eigenvalues of $M(\mathbf{q})$ are $\lambda_\pm = iKq_x \pm Kq_y$. The crystal is therefore unstable as soon as $q_y \neq 0$. Secondly, it is worth noting that this linear dynamics was conjectured in (12) to model crystals driven through a frictional medium. The above analysis shows that this simplified model does not correctly account for the dynamics of 2D crystals driven through confined viscous fluids.

C. Long-range dipolar interaction: F^{NR} and dislocation dynamics.

C.1. Computation of \mathbf{F}^{NR} . In this section we compute the non-reciprocal force field F^{NR} that arises from microscopic hydrodynamic interactions relevant to our experiments. We recall that these microscopic forces are long ranged and have a dipolar symmetry, they take the form:

$$\mathbf{F}(\mathbf{r}) = \frac{-\sigma}{r^2} \begin{pmatrix} \cos(2\theta) \\ \sin(2\theta) \end{pmatrix}. \quad [54]$$

As detailed in above, the linear dynamics of the displacement field is given by

$$\zeta \partial_t \tilde{\mathbf{u}}(\mathbf{q}) = M(\mathbf{q}) \cdot \tilde{\mathbf{u}}(\mathbf{q}), \quad [55]$$

where the stability matrix is

$$M(\mathbf{q}) = -\frac{i\pi\sigma\bar{\rho}}{2} q \begin{pmatrix} \cos(3\varphi) & \sin(3\varphi) \\ \sin(3\varphi) & -\cos(3\varphi) \end{pmatrix}. \quad [56]$$

Equivalently, in real space the crystal dynamics then takes the form $\partial_t \mathbf{u}(\mathbf{r}) = \mathbf{F}^{\text{NR}}(\{\mathbf{u}(\mathbf{r})\})$, where $\mathbf{F}^{\text{NR}}(\{\mathbf{u}(\mathbf{r})\})$ is a non-local function of the strain field as a result of the long-range nature of the interactions. Computing the Fourier transform of $M(\mathbf{q})$, we obtain

$$\mathbf{F}^{\text{NR}}(\{\mathbf{u}(\mathbf{r})\}) = \int d\mathbf{r}' M(\mathbf{r} - \mathbf{r}') \cdot \mathbf{u}(\mathbf{r}'), \quad [57]$$

$$M_{kl} = -\bar{\rho} \frac{\partial F_k}{\partial r_l}, \quad [58]$$

$$\nabla \mathbf{F} = \frac{2\sigma}{r^3} \begin{pmatrix} \cos(3\theta) & \sin(3\theta) \\ \sin(3\theta) & -\cos(3\theta) \end{pmatrix}. \quad [59]$$

At this stage it is worth noting that \mathbf{F}^{NR} is nothing else but the convolution of the microscopic dipolar force \mathbf{F} with the local density fluctuation $\delta\rho \simeq -\bar{\rho} \nabla \cdot \mathbf{u}$. This can be readily seen by writing

$$F_k^{\text{NR}} = -\bar{\rho} \int d\mathbf{r}' \frac{\partial F_k}{\partial r_l}(\mathbf{r} - \mathbf{r}') u_l(\mathbf{r}') = -\bar{\rho} \int d\mathbf{r}' F_k(\mathbf{r}') \frac{\partial u_l}{\partial r_l}(\mathbf{r} - \mathbf{r}'), \quad [60]$$

$$\mathbf{F}^{\text{NR}}(\{\mathbf{u}(\mathbf{r})\}) = -\bar{\rho} \int d\mathbf{r}' \mathbf{F}(\mathbf{r}') \nabla \cdot \mathbf{u}(\mathbf{r} - \mathbf{r}'). \quad [61]$$

This result will prove very useful to address the dynamics of an isolated dislocation below.

C.2. Computation of $\dot{\mathbf{u}}^{\text{NR}}$ around an isolated dislocation. We now compute the velocity field induced by the nonreciprocal forces around an isolated dislocation at the origin. It corresponds to $\dot{\mathbf{u}}^{\text{NR}}$ defined in the main text. We define the Burgers vector of the dislocation $\mathbf{b} = b\hat{\mathbf{e}}_\beta$ as $\oint \partial_i u_j dr_i = b_j$. When the particle forming the lattice are elastically coupled a dislocation induces displacements that decay algebraically as

$$\mathbf{u}(\mathbf{r}) = \frac{b}{2\pi} \left[\theta \begin{pmatrix} \cos \beta \\ \sin \beta \end{pmatrix} + \frac{1-\nu}{2} \log r \begin{pmatrix} \sin \beta \\ -\cos \beta \end{pmatrix} + \frac{1+\nu}{2} \cos(\theta - \beta) \begin{pmatrix} \sin \theta \\ -\cos \theta \end{pmatrix} \right] \quad [62]$$

where ν is the Poisson ratio. The corresponding deformations read

$$\frac{\partial u_x}{\partial x} + \frac{\partial u_y}{\partial y} = \frac{b(1-\nu)}{2\pi r} \sin(\beta - \theta), \quad \frac{\partial u_x}{\partial y} - \frac{\partial u_y}{\partial x} = \frac{b}{\pi r} \cos(\theta - \beta), \quad [63]$$

$$\frac{\partial u_x}{\partial x} - \frac{\partial u_y}{\partial y} = -\frac{b(1+\nu)}{2\pi r} \cos(\theta - \beta) \sin(2\theta), \quad \frac{\partial u_x}{\partial y} + \frac{\partial u_y}{\partial x} = \frac{b(1+\nu)}{2\pi r} \cos(\theta - \beta) \cos(2\theta), \quad [64]$$

We can now use Eq. (60) to compute $\dot{\mathbf{u}}^{\text{NR}}$. The convolution product is easily evaluated in Fourier space: $\tilde{\mathbf{u}}^{\text{NR}}(\mathbf{q}) = \zeta^{-1} \tilde{\mathbf{F}}^{\text{NR}}(\mathbf{q}) = \zeta^{-1} \delta \tilde{\rho}(\mathbf{q}) \tilde{\mathbf{F}}(\mathbf{q})$. We find

$$\tilde{\mathbf{u}}^{\text{NR}}(\mathbf{q}) = i\zeta^{-1} b\pi^2 (1-\nu) \sigma \bar{\rho} \frac{\sin(\beta - \varphi)}{q} \begin{pmatrix} \cos(2\varphi) \\ \sin(2\varphi) \end{pmatrix}, \quad [65]$$

where we have used

$$\tilde{\mathbf{F}}(\mathbf{q}) = \int_0^\infty dr r \int_0^{2\pi} d\theta e^{-iqr \cos(\theta - \varphi)} \frac{-\sigma}{r^2} \begin{pmatrix} \cos(2\theta) \\ \sin(2\theta) \end{pmatrix} = \pi \sigma \begin{pmatrix} \cos(2\varphi) \\ \sin(2\varphi) \end{pmatrix}, \quad [66]$$

and

$$\delta \tilde{\rho}(\mathbf{q}) = -\bar{\rho} \int_0^\infty dr r \int_0^{2\pi} d\theta e^{-iqr \cos(\theta - \varphi)} \frac{b(1-\nu)}{2\pi r} \sin(\beta - \theta) = ib(1-\nu)\pi \frac{\sin(\beta - \varphi)}{q}. \quad [67]$$

We can then express the flow field in real space and find

$$\dot{\mathbf{u}}^{\text{NR}}(\mathbf{r}) = i\zeta^{-1} b\pi^2 (1-\nu) \sigma \bar{\rho} \frac{1}{(2\pi)^2} \int_0^\infty dq q \int_0^{2\pi} d\varphi e^{+iqr \cos(\varphi - \theta)} \frac{\sin(\beta - \varphi)}{q} \begin{pmatrix} \cos(2\varphi) \\ \sin(2\varphi) \end{pmatrix} \quad [68]$$

$$= \frac{\pi \zeta^{-1} b(1-\nu) \sigma \bar{\rho}}{2r} \cos(\beta - \theta) \begin{pmatrix} -\sin(2\theta) \\ \cos(2\theta) \end{pmatrix}. \quad [69]$$

This far-field calculation captures well the symmetries and the decay of the sum of all the microscopic forces as shown in Fig. S5A-B. Before explaining how this force field drives the motility and splitting of the dislocations we can make two side comment. We note that point defects such as interstitials also induce a nontrivial force field on the surrounding particles. Following the same procedure as above, we find that it has a dipolar symmetry too. It is well described by Eq. (40), \mathbf{r} being now the distance to the defect core. The same results holds for vacancies for which Eq. (40) has to be corrected by a sign factor.

Lastly it is worth noting that the symmetries of the flows induced by dipolar interactions around a dislocation (Eq. Eq. (69)) are robust to the interaction range. Considering screened dipolar interactions (see Section B), we can combine Eq. (53) and Eq. (64) to find that they yield $\dot{\mathbf{u}}^{\text{NR}}$ flows having the same symmetries as in Fig. S5A-B, see also (11).

D. Effective Peach-Koehler force. Fig. S5A shows that the hydrodynamic forces, if unopposed, would lead to shear and/or dilation deformations. But as they are opposed by elastic forces, they translate into shear and dilation stresses within the crystal. Instead of using the kinematic arguments from the main text to account for the dislocation dynamics, we can instead opt for the classical Peach-Koehler-force argument (15). In short, a dislocation of Burgers vector \mathbf{b} in an external stress field $\boldsymbol{\sigma}$ can release elastic energy by moving. The energy gain per unit distance translates into a force commonly referred to as the Peach-Koehler force \mathbf{F}^{PK} . It takes the form

$$F_i^{\text{PK}} = \epsilon_{ij} \sigma_{kj} b_k, \quad [70]$$

where ϵ_{ij} is the totally antisymmetric tensor (13, 15). This force is of purely topological origin and does not depend on the specifics of the constitutive relation that relates the stress to the strain field.

When the magnetic interactions are strong, our system is an elastic material driven by a self-induced non-reciprocal-force field \mathbf{F} , Eq. (69). We showed in (11) that we can estimate the magnitude of the effective Peach-Koehler force that arise from the hydrodynamic forces as

$$F_i^{\text{PK}} = \epsilon_{ij} \left. \frac{\partial F_k^{\text{NR}}}{\partial r_j} \right|_{\text{disloc}} b_k, \quad [71]$$

where $\left. \frac{\partial F_k^{\text{NR}}}{\partial r_j} \right|_{\text{disloc}}$ defines the force difference across the dislocation, it plays the role of an effective stress acting on it. In Ref. (11), we showed how to estimate this force gradient and found

$$\left. \frac{\partial F_i}{\partial r_j} \right|_{\text{disloc}} = \frac{f_0}{b} \begin{pmatrix} -\sin \beta & -\cos \beta \\ \cos \beta & -\sin \beta \end{pmatrix} \quad [72]$$

where f_0 is a constant having the dimension of a force, β is the orientation of the Burgers vector. Introducing this expression into Eq. (71), we find a simple expression for the effective Peach-Koehler force acting on the dislocation:

$$\mathbf{F}^{\text{PK}} = -f_0 \hat{\mathbf{e}}_x. \quad [73]$$

It is always oriented in the direction opposite to the flow that induces the dipolar interactions, and is independent of the orientation of the Burgers vector (Fig. S5B).

E. Gliding, climbing and splitting. \mathbf{F}^{PK} tells us that some elastic energy is gained when the dislocation moves towards the left hand side. But it doesn't say whether this motion is possible and does not specifies its kinematics either. It is standard to distinguish the motion of the dislocation along its Burgers vector, known as glide motion, from a motion orthogonal to the Burgers vector, known as climb motion (16). While glide is easily achieved by local rearrangements around the dislocation, climb is usually forbidden microscopically. It can happen only directly with a transfer of mass, or effectively by the splitting of the dislocation in two gliding dislocations (17). We investigate the relevance of gliding and climbing scenarios in the dynamics that we observe. To do this, we first decompose the effective Peach-Koehler force, Eq. (73), on the basis made by the normalized Burgers vector $\hat{\mathbf{b}} = \mathbf{b}/b$ and its orthogonal vector $\hat{\mathbf{b}}^\perp$ ($\hat{b}_i^\perp = -\epsilon_{ij}\hat{b}_j$) (see also Fig. S5B):

$$\mathbf{F}^{\text{PK}} = \mathbf{F}_{\text{glide}}^{\text{PK}} + \mathbf{F}_{\text{climb}}^{\text{PK}}, \quad [74]$$

$$\mathbf{F}_{\text{glide}}^{\text{PK}} = (\mathbf{F}^{\text{PK}} \cdot \hat{\mathbf{b}}) \hat{\mathbf{b}} = -f_0 (\hat{\mathbf{b}} \cdot \hat{\mathbf{e}}_x) \hat{\mathbf{b}}, \quad [75]$$

$$\mathbf{F}_{\text{climb}}^{\text{PK}} = (\mathbf{F}^{\text{PK}} \cdot \hat{\mathbf{b}}^\perp) \hat{\mathbf{b}}^\perp = -f_0 (\hat{\mathbf{b}}^\perp \cdot \hat{\mathbf{e}}_x) \hat{\mathbf{b}}^\perp. \quad [76]$$

Glide. Let us focus on the glide component first (Eq. (75)). As seen in our numerical simulations, this is the main direction in which the dislocations move, Fig. S5C. The amplitude of the glide force is proportional to $|\cos \beta|$ where β is the angle of the Burgers vector with the horizontal axis. More relevant is the speed at which a gliding dislocation moves in the x direction. Its speed is proportional to $-\cos^2 \beta$, in agreement with our numerical simulations, see Fig. S5F.

Instead of the effective Peach-Koehler argument, one may adopt a purely kinematic perspective on the glide of the dislocations as in the main text. Microscopically, glide happens if particles above and below the glide line are driven in opposite directions (parallel the glide line). Noting $\dot{\mathbf{u}}^{\text{NR}}$ the velocity imposed by the hydrodynamic forces its component along the glide line is $\dot{\mathbf{u}}^{\text{NR}} \cdot \hat{\mathbf{b}}$. Writing the gradient perpendicular to the glide line as $\hat{\mathbf{b}}^\perp \cdot \nabla$, we conclude that the component of the velocity field $\dot{\mathbf{u}}^{\text{NR}}$ that powers motion is $\hat{\mathbf{b}}^\perp \cdot \nabla (\dot{\mathbf{u}}^{\text{NR}} \cdot \hat{\mathbf{b}})$. This kinematic reasoning (which particles move in which direction) gives an equivalent perspective as the Peach-Koehler argument.

We note that at strong magnetic fields in our numerical simulations, gliding dislocations actually favor the ordering of the system since two of them can collide and annihilate or merge into a single one (see Fig. 3I of the main text, showing a circular grain boundary as initial condition).

Climb. The amplitude of the climb force, Eq. (76), is proportional to $|\sin \beta|$. In practice, a dislocation cannot move in this direction because this would require a mass transfer between above and below the glide plane. An alternative scenario, clearly illustrated in Ref. (17), was dubbed “climbing by gliding”. It involves first the splitting of the dislocation into a pair of dislocations (with conservation of the total vector charge) and then the gliding of these two dislocations which have glide planes different from the one of the original dislocation. This scenario is observed in our numerical simulations, see Fig. 5B. It provides a basis for the splitting, and by extension the proliferation of dislocations leading to the melting of the system when the magnetic interactions are weak enough.

F. Grain boundaries. The phenomenology that we observe for isolated dislocations in our numerical simulations also holds for grain boundaries. In particular, (straight) grain boundaries move upstream, see Fig. 3E of the main text and Fig. S5D-E. This is not surprising since an interface between two crystals with a finite angle mismatch is nothing but a line of well separated dislocations (the value of the angle mismatch defines the line density of the dislocation along the grain boundary). These dislocations glide upstream together so that the grain boundary globally translates in this direction. (We recall that the angle mismatch $\Delta\theta_6 \in [-30^\circ, 30^\circ]$ is defined as the difference between the phases θ_6 of the hexatic order parameter in the two phases).

The dependence of the speed of a grain boundary, as a function of its orientation from the horizontal axis is similar to an isolated dislocation's, but with a smaller prefactor, see Fig. S5F.

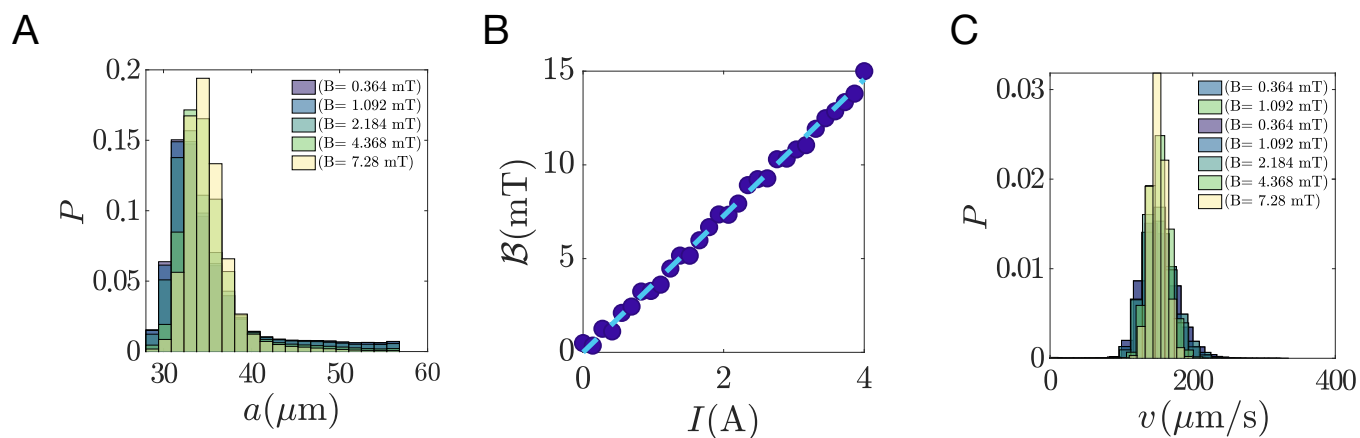


Fig. S1. Controlling the production of a magnetic soft crystal

A. The radius of droplets does not vary with B . **B.** Variations of the B field strength with the intensity of the current in the coil. **C.** Velocity distributions of the droplets for different applied magnetic field. No crucial difference is observed in the velocity distribution of the droplets.

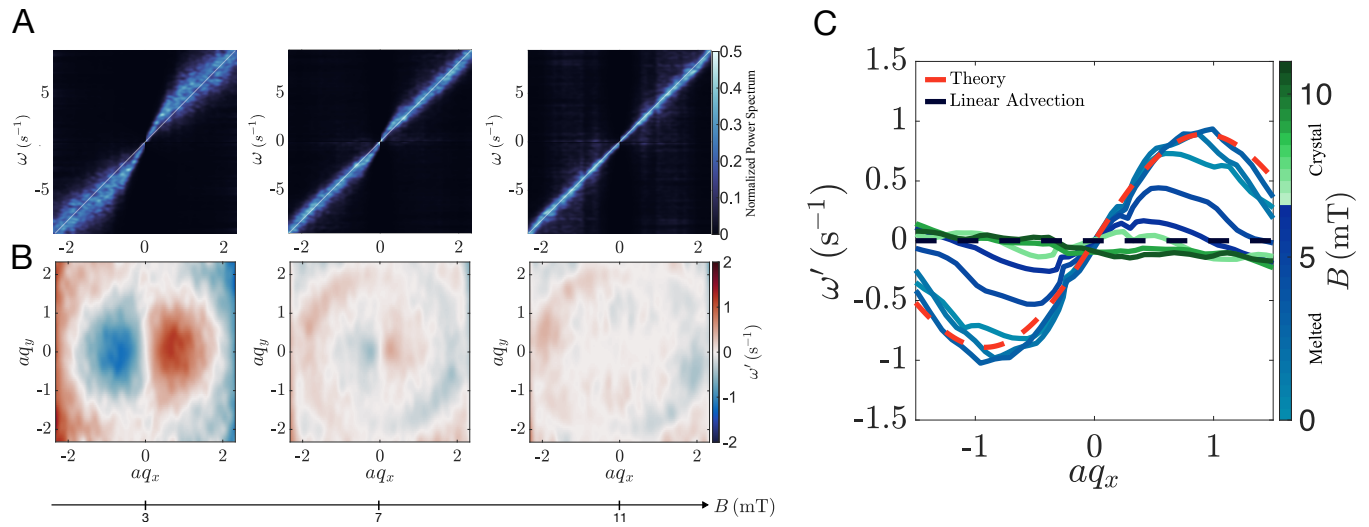


Fig. S2. Sound waves and dispersion relations

A. Power spectra $\mathcal{P}_\rho(q_x, q_y = 0, \omega)$ plotted for different values of B . In the liquid phase dispersive density waves propagate through the emulsion. Deep in the crystal phase, the density fluctuations are merely advected with the crystal. **B.** Dispersion relations on the density waves in the frame moving with the center of mass of the emulsion ($\omega' = \omega - Uq_x$). Same values of B as in **A.** **C.** Cut of the dispersion relation in the $q_y = 0$ plane and comparison to theory (7).

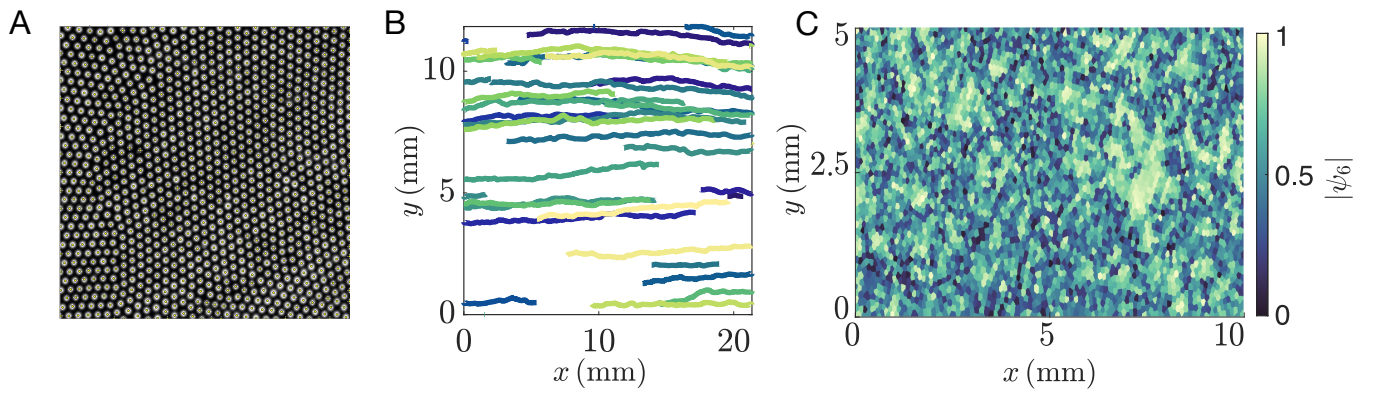


Fig. S3. Particles tracking and field reconstruction

A. Particles detection : we detect the center of mass of all droplets in the field of view using the ImageJ minima intensity detection function on contrast-enhanced and Gaussian blurred frames (the SD of the Gaussian kernel is taken roughly equal to $a/2$) **B.** We reconstruct the drop trajectories and measure their instantaneous velocity using the MATLAB function based on the Crocker and Grier tracking algorithm. **C.** Eulerian ψ_6 field in the observation region ($B = 5$ (mT)) computed from the droplet instantaneous positions. We ensure that no large density fluctuation or packing fraction occurs in the observed region.

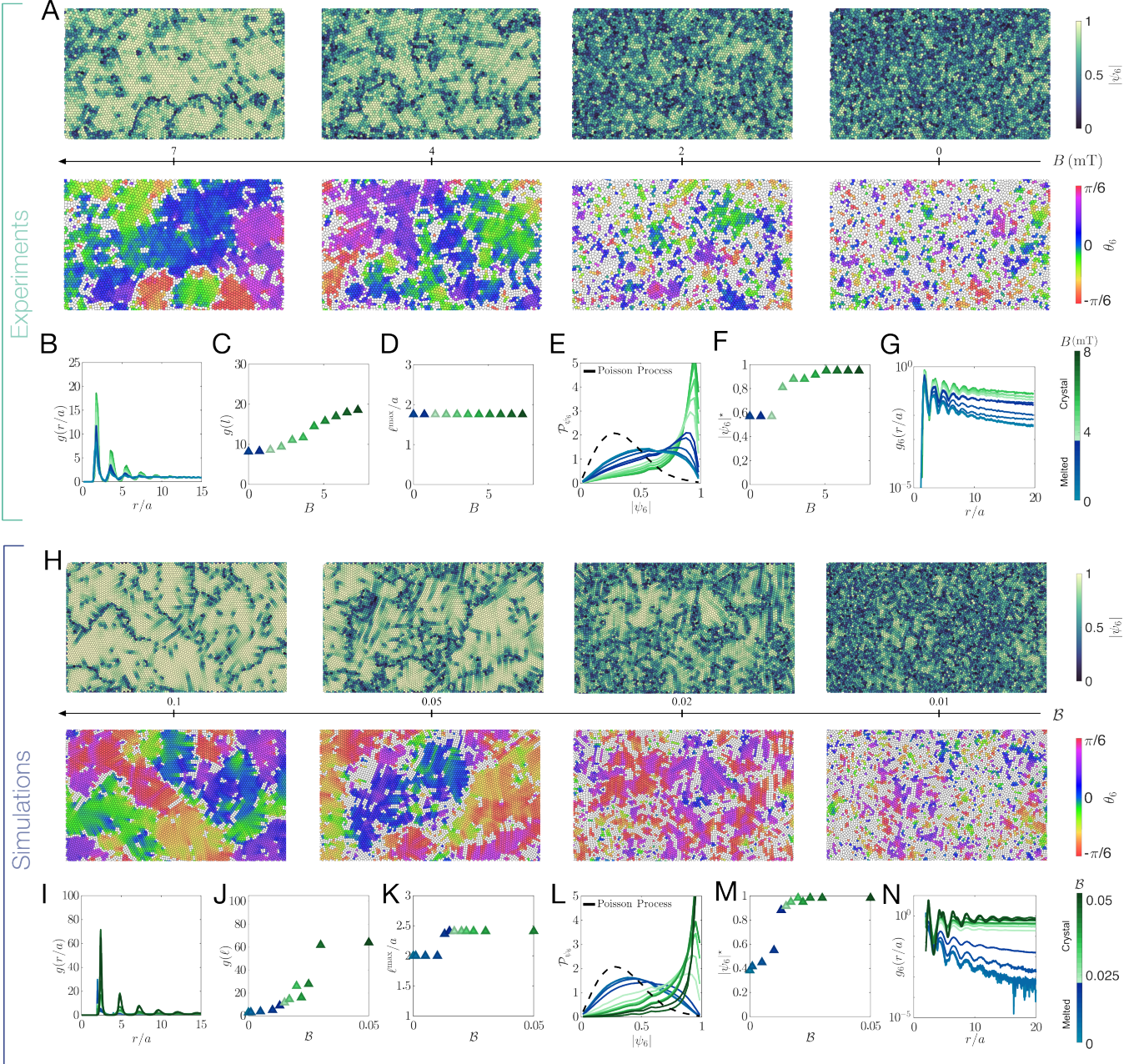


Fig. S4. Hydrodynamic melting ($\phi = 0.61$)

A. Maps of $|\psi_6|$ and θ_6 for four different values of B . Packing fraction $\phi_1 = 0.61$. We observe a melting phenomenology similar to that reported for $\phi_2 = 0.33$ in the main text. **B.** Pair correlation functions $g(r/a)$ measured along the direction defined by the local value of θ_6 . $g(r/a)$ is plotted for different values of the applied magnetic field. The inner structure of the crystal clusters hardly evolves as B decreases. **C.** Variations of the amplitude of the first crystal peak $g(\ell)$ with B . **D.** The position of the first peak of $g(r/a)$ (ℓ) does not vary with B . The structure of the Wigner crystals does not change in the bulk as B decreases. **E.** Distribution of the magnitude of the local and instantaneous hexatic field $\psi_6(\mathbf{r}, t)$. Dashed line same distribution computed for a Random set of points (2D Poissonian process). **F.** Evolution of the position of the maximum of the ψ_6 distribution with the magnitude of the repulsive interactions. The position of the ψ_6 maximum clearly signals the melting point of the polycrystal structure. **G.** Spatial correlations of ψ_6 (**H-N**). Comparison to numerical simulations

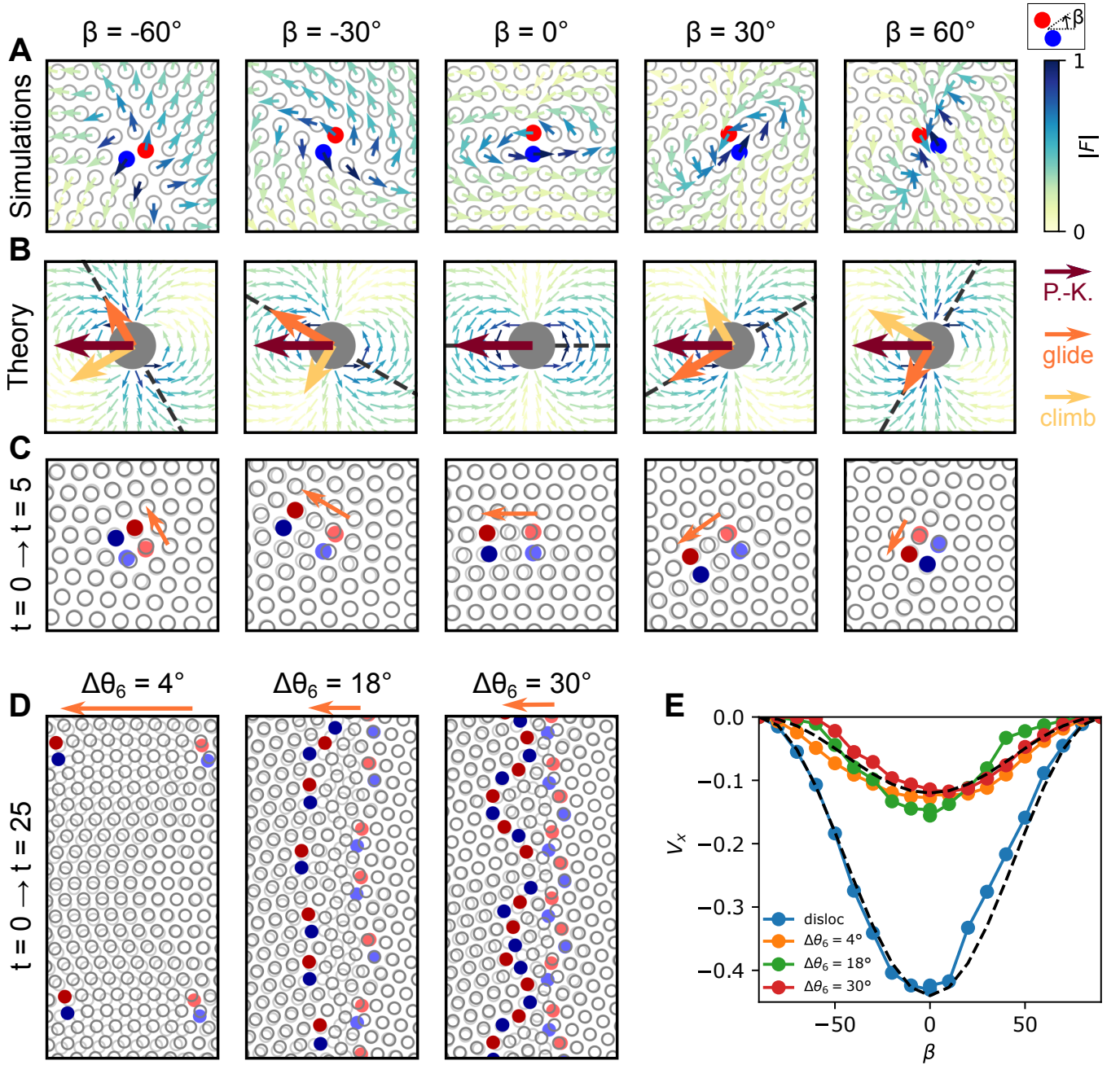


Fig. S5. Peach-Koehler force and dislocation glide.

A. Dislocation with a Burgers vector at angle β with the horizontal axis ($\beta = -60^\circ, -30^\circ, 0^\circ, 30^\circ, 60^\circ$). The red (resp. blue) filled particle has 5 (resp. 7) neighbors. The arrows are the hydrodynamic forces \mathbf{F}_i acting on each particle (the norm is coded by the colormap). **B.** Depiction of the theoretical force field, $F(r, \theta)$, from Eq. (69) with the same colormap. We see a good agreement with the microscopic forces in panel A. The dashed line is the glide line of the dislocation. The three arrows depict the effective Peach-Koehler force (Eq. (73)), its glide component and its climb component (darker to lighter colors). **C.** When the initial condition is evolved with additional strong magnetic interactions ($B = 0.2$), the dislocation always glide towards the left, as expected. The initial state ($t = 0$) is shown with light red, blue and grey colors, while the state at $t = 0$ is shown with dark colors. The arrow indicate the glide of the dislocation. **D.** Flat grain boundaries with mismatch angles $\Delta\theta_6 = 18^\circ$ and 30° shown between $t = 0$ and $t = 25$, with the same convention as panel C. The angle of the grain compared to the horizontal axis is $\beta = 0$. **E.** Steady-state velocity V_x along the x -axis for an isolated dislocation and grain boundaries with mismatches $\Delta\theta_6 = 4^\circ, 18^\circ$ and 30° , as a function of the angle β with the horizontal axes. The dashed lines show dependencies as $-\cos^2 \beta$ predicted by our theory.

Movie S1. Steady state dynamics of a driven polycrystal (experiments). This movie shows the spatio-temporal variations of the θ_6 field measured in an experiment where $B = 9.7 \text{ mT}$ and $\phi = 0.37$. θ_6 is measured in each Voronoi cell, constructed from the positions of the individual droplets. Grain boundaries are defined as regions where the magnitude of the order parameter falls below a threshold of $|\psi_6| < 0.6$. The nonreciprocal forces continuously reshape the grain boundary network. (Video recorded at 2 fps, played at 50 fps.)

Movie S2. Hydrodynamic melting (experiments). Hydrodynamic melting. These four videos show the spatio-temporal variations of the hexatic order parameter for four different values of the B field (packing fraction $\phi = 0.37$). The videos demonstrate the transition from an ordered polycrystal (high ψ_6 values) to a disordered liquid state (low ψ_6 values). Video recorded at 10 fps, played at 2 fps.

Movie S3. Motile grain boundary (simulations). This movie shows the simulated dynamics of straight grain boundary. The nonreciprocal interactions do not alter the shape of the interfaces between the two crystals but propel them in the upstream direction. ($B = 0.2$). The color indicates the orientation of the crystals. The Voronoi cells are filled with a white color when the orientational order parameter ψ_6 is smaller than 0.6.

Movie S4. Dynamics of a circular grain (Simulations). This movie shows that circular grain boundaries are not merely propelled by nonreciprocal forces. The circular shape is not stable ($B = 0.2$). The color indicates the local orientation of the crystals (θ_6 field).

Movie S5. Dislocations proliferate at grain boundaries (Simulations). This video shows the structural evolution of two crystals separated by a straight grain boundary after a rapid quench of B . The initial condition corresponds to an configuration that minimizes the conservative interactions between the particles. We then quench the system by turning on the nonreciprocal forces ($B = 0.005$) below the melting threshold. The movie shows that the dislocations at the interface propel, interact and proliferate while the bulk of the crystals remain stable.

Movie S6. Nonreciprocal forces propel and fission dislocations (Simulations). An isolated dislocation glide and fission. The resulting pair of dislocations glide, interact and then proliferates throughout the sample, leading to a steady state dynamics where small grains are surrounded by a liquid phase ($B = 0.005$).

References

1. D Bartolo, G Degre, P Nghe, V Studer, Microfluidic stickers. *Lab on a chip* **8**, 274–9 (2008).
2. B Levaché, A Azioune, M Bourrel, V Studer, D Bartolo, Engineering the surface properties of microfluidic stickers. *Lab Chip* **12**, 3028–3031 (2012).
3. KA Materials, Su-8 2000 permanent negative epoxy photoresist (2020).
4. AT Skjeltorp, One- and two-dimensional crystallization of magnetic holes. *Phys. Rev. Lett.* **51**, 2306–2309 (1983).
5. J Crocker, D Grier, Methods of digital video microscopy for colloidal studies. *J. Colloid Interface Sci.* **179**, 298–310 (1996).
6. T Beatus, T Tlusty, R Bar-Ziv, Phonons in a one-dimensional microfluidic crystal. *Nat. Phys.* **2**, 743–748 (2006).
7. N Desreumaux, JB Caussin, R Jeanneret, E Lauga, D Bartolo, Hydrodynamic fluctuations in confined particle-laden fluids. *Phys. Rev. Lett.* **111** (2013).
8. T Beatus, I Shani, RH Bar-Ziv, T Tlusty, Two-dimensional flow of driven particles: a microfluidic pathway to the non-equilibrium frontier. *Chem. Soc. Rev.* **46**, 5620–5646 (2017).
9. I Saeed, HK Pak, T Tlusty, Quasiparticles, flat bands and the melting of hydrodynamic matter. *Nat. Phys.* **19**, 536–544 (2023).
10. D Frenkel, B Smit, *Understanding molecular simulation: from algorithms to applications*. (Elsevier) Vol. 1, (2001).
11. A Poncet, D Bartolo, When soft crystals defy newton’s third law: Nonreciprocal mechanics and dislocation motility. *Phys. Rev. Lett.* **128**, 048002 (2022).
12. R Lahiri, S Ramaswamy, Are steadily moving crystals unstable? *Phys. Rev. Lett.* **79**, 1150–1153 (1997).
13. P Oswald, *Rheophysics*. (Cambridge University Press), (2009).
14. T Tlusty, Exceptional topology in ordinary soft matter. *Phys. Rev. E* **104**, 025002 (2021).
15. M Peach, JS Koehler, The forces exerted on dislocations and the stress fields produced by them. *Phys. Rev.* **80**, 436–439 (1950).
16. LD Landau, EM Lifshitz, *Theory of elasticity*. (Pergamon Press, Oxford New York), (1986).
17. WTM Irvine, AD Hollingsworth, DG Grier, PM Chaikin, Dislocation reactions, grain boundaries, and irreversibility in two-dimensional lattices using topological tweezers. *Proc. Natl. Acad. Sci.* **110**, 15544–15548 (2013).